Available online at www.sciencedirect.com
ScienceDirect
Acta Materialia 55 (2007) 2863–2873
Acta MATERIALIA
www.actamat-journals.com

Forming limits for electromagnetically expanded aluminum alloy tubes: Theory and experiment

J.D. Thomas [a], M. Seth [b], G.S. Daehn [b], J.R. Bradley [c], N. Triantafyllidis [a,*]

[a] The University of Michigan, Aerospace Engineering Department, Ann Arbor, MI 48109-2140, USA
[b] The Ohio State University, Materials Science and Engineering Department, Columbus, OH 43210, USA
[c] General Motors R&D Center, Materials and Processes Laboratory, Warren, MI 48090-9055, USA

Received 19 April 2006; received in revised form 14 December 2006; accepted 19 December 2006
Available online 28 February 2007

Abstract

The electromagnetic forming process is a high-velocity manufacturing technique which uses electromagnetic (Lorentz) body forces to shape sheet metal parts. One of the several advantages of this technique is the considerable ductility increase observed in several metals, with aluminum featuring prominently among these. Motivated by the quasistatic case, recent work has extended the concept of forming limit diagrams (FLDs) to model the ductility of electromagnetically formed sheets. This general theory is hereby applied to study the ductility of freely expanding electromagnetically loaded aluminum tubes. Necking strains are measured in tubes of various geometries which are loaded by different coils and currents. The experimental results are plotted in principal strain space and show reasonable agreement with the corresponding theoretical FLD predictions, which indicate a 2- to 3-fold increase in the forming limits with respect to the quasistatic case.

Keywords: Aluminum alloys; Ductility; High-speed deformation; Electromagnetic process

1. Introduction

High-velocity electromagnetic forming (EMF) can be a flexible and cost-effective alternative to conventional metal stamping and forming processes. Electromagnetic forming is accomplished by connecting an actuator (typically a solenoid coil consisting of copper windings) in series with a high-energy capacitor bank. Upon discharging the capacitor, a large current runs through the actuator and induces currents in the metallic workpiece. The presence of these induced currents inside the magnetic field of the actuator results in Lorentz body forces in the workpiece that can be made to cause plastic deformation. The EMF technique is particularly attractive for the aerospace and automotive industries due to several potential advantages over conventional forming methods: low-cost single-side tooling, high speed (typical EMF current pulse rise times are on the order of 20 μs and after electromagnetic launch deformation may persist for a time on the order of milliseconds) and precise process control.

The main reason for interest in EMF is the resulting significant increase in ductility observed in certain metals, with aluminum being the most prominent among these. Experimental work by Balanethiram and Daehn [1,2] with die impact EMF has resulted in forming limit diagrams (FLDs) that show dramatic increases (compared to conventional hydroforming) in the ductility of the EMF formed AA6061-T4, thus making aluminum alloys possibly more ductile than conventional mild steel. A theoretical explanation of this observed increase in formability based on fully coupled electromagnetic and thermomechanical modeling of EMF ring free expansion was recently provided by Triantafyllidis and Waldenmyer [3]. It was shown that the strain rate sensitivity occurring in aluminum alloys

* Corresponding author. Tel.: +1 734 763 2356; fax: +1 734 763 0578.
E-mail address: nick@umich.edu (N. Triantafyllidis).

1359-6454/$30.00
doi:10.1016/j.actamat.2006.12.025

at high EMF strain rates is the main mechanism responsible for the observed higher necking strains of the ring.

Further recent work [4–11] has examined high strain rate (EMF and non-EMF) free forming limits. Oliveira and Worswick [9] and Oliveira et al. [10] showed that there was little increase in ductility due to high EMF strain rates, and Oosterkamp et al. [12] demonstrated minimal strain rate sensitivity in aluminum. The work by Oosterkamp et al. [12] used a split Hopkinson pressure bar to examine strain rates up to $2\times10^3\ s^{-1}$, with a moderate number of data points, and reported that apparent strain rate sensitivity is an artefact and not inherent in the material. However, other work, such as that by Hu and Daehn [5], indicates that high strain rate free formability increases, and Vural et al. [13] and Yadav et al. [14] showed that there was significant strain rate sensitivity in aluminum. In particular, Vural et al. [13] used the shear compression specimen technique (e.g. see [15]) to give extensive data for AA6061-T6 up to strain rates on the order of $10^4\ s^{-1}$. These data show distinct strain rate sensitivity above $10^3\ s^{-1}$. Also, several of the above-mentioned recent investigations [4,5,7,8,11] show theoretically that inertial effects can delay instability. These investigations also point to the fact that the physical dimensions of the sample affect strains to instability and rupture.

A question that naturally follows is how to apply the work in modeling the ring experiment to more complicated EMF structures to allow comparison with experiments and further investigate formability mechanisms. The consistent approach must involve, as in the ring work [3], the fully coupled electromagnetic and mechanical modeling of the actuator and the workpiece. This is a computationally intensive process that requires the development of sophisticated algorithms for the solution of a dynamic finite strain thermoplasticity boundary value problem coupled (in view of the driving Lorentz body forces) to an electromagnetic problem with moving boundaries. Although this direct approach is the correct way for accurate calculations of specific EMF processes (with known part and actuator geometries), the designer can be helped by some simpler, and considerably more rapid, calculations that give a reasonable estimate of the ductility of a given alloy under EMF conditions. With this requirement in mind, Thomas and Triantafyllidis [16] have recently proposed a general theory to calculate EMF-based FLDs, in which the calculation of strains at the onset of necking in a sheet accounts for the presence of electric currents and the resulting ohmic heating effect.

The present work pertains to the comparison of theoretical simulations based on Thomas and Triantafyllidis [16] with experimental data obtained from a series of experiments on electromagnetically expanded aluminum alloy tubes. In Section 2, a brief description of the necking analysis for EMF-based processes proposed in Thomas and Triantafyllidis [16] is followed by discussions of the experimental procedure, the selection of material properties for the AA6063-T6 tube alloy, and a description of the strain and current density profiles. Following a short description of the numerical solution algorithm for the onset of necking problem, the results of four different experiments are presented, compared to the corresponding theoretical simulations and discussed in Section 3. Conclusions are given in Section 4.

2. Problem formulation

The ductility prediction of an electromagnetically free formed sheet (i.e. by using a process that does not involve die impact) will be based on a forming limit diagram concept that is widely used in the analysis of conventional (i.e. purely mechanical) sheet metal forming processes. The general theory of the EMF-based FLD has been proposed by Thomas and Triantafyllidis [16] and is recorded here for reasons of completeness. The formulation starts with the "weak band" analysis for the localization of deformation in a biaxially stretched sheet subjected to electric currents. The section continues with the presentation of temperature-dependent viscoplastic constitutive models for the sheet and ends by introducing the strain and current profiles adopted for modeling the EMF process.

2.1. Localization of deformation analysis

By ignoring curvature and inertia effects, the sheet is idealized as a thin plate under plane stress conditions, as depicted in Fig. 1. It is assumed that deformation is localized in a narrow band B with normal $\boldsymbol{N}=\boldsymbol{i}\cos\Phi+\boldsymbol{j}\sin\Phi$ and tangent $\boldsymbol{S}=-\boldsymbol{i}\sin\Phi+\boldsymbol{j}\cos\Phi$ in the reference, stress-free configuration. The quantities in the current configuration are denoted by the corresponding script symbols $\boldsymbol{n}$, $\boldsymbol{s}$ and ϕ. The band (B) is distinguished from the sheet (A) by the presence of an initial imperfection, which is implemented as a discontinuity in the reference configuration, either of a material or a geometric (thickness) parameter. The goal is to calculate the deformation gradient $\boldsymbol{F}^B$, stresses $\boldsymbol{\sigma}^B$, currents $\boldsymbol{j}^B$, temperature θ^B and internal variable (plastic strain) ϵ_B^{p} inside the band given the knowledge of the counterpart of those quantities outside the band $\boldsymbol{F}^A$, $\boldsymbol{\sigma}^A$, $\boldsymbol{j}^A$, θ^A and ϵ_A^{p}.

A full Lagrangian (reference configuration) formulation of the problem is hereby adopted. For simplicity only incompressible materials are considered, which is a realistic

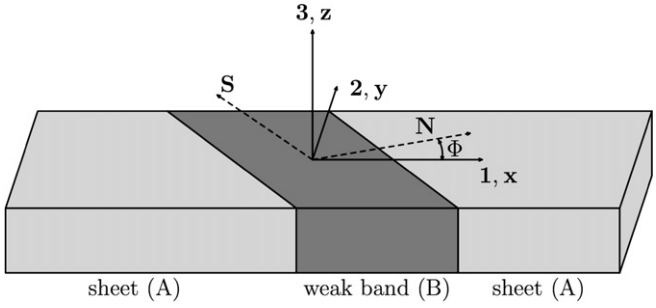

Fig. 1. The weak band model showing band orientation in the reference configuration.

approximation for metals under high strains. Mechanics dictates displacement and traction continuity. Displacement continuity across the band gives[1]

$$[F^B_{\alpha\beta} - F^A_{\alpha\beta}]S_\beta = 0, \tag{2.1}$$

while traction continuity across the band implies

$$N_\alpha[\Pi^B_{\alpha\beta} - \Pi^A_{\alpha\beta}] = 0, \tag{2.2}$$

where $\boldsymbol{\Pi}$ is the first Piola–Kirchhoff (P–K) stress. For an incompressible solid the first P–K stress is related to the Cauchy stress by

$$\Pi_{ij} = F^{-1}_{ik}\sigma_{kj}. \tag{2.3}$$

Electrical principles require continuity of the current and of the tangential component of the electromotive force across the band. Current continuity gives

$$N_\alpha[J^B_\alpha - J^A_\alpha] = 0, \tag{2.4}$$

where $\boldsymbol{J}$ is the current density vector in the reference configuration. For an incompressible solid $\boldsymbol{J}$ is related to $\boldsymbol{j}$, its counterpart in the current configuration, by

$$J_i = F^{-1}_{ij} j_j. \tag{2.5}$$

Continuity of the tangential component of the electromotive force $\boldsymbol{E}$ across the band requires

$$S_\alpha[E^B_\alpha - E^A_\alpha] = 0, \tag{2.6}$$

where the reference configuration electromotive force $\boldsymbol{E}$ is related to its current configuration counterpart $\boldsymbol{e}$ by

$$E_i = e_j F_{ji}. \tag{2.7}$$

Finally, from energy conservation, assuming that adiabatic heating takes place in the sheet both inside (B) and outside (A) the weak band (hence no need for indexing the various field quantities), one has for an incompressible solid

$$\mu c_p \dot{\theta} = \chi \sigma_e \dot{\epsilon}^p + E_i J_i, \tag{2.8}$$

where μ is the mass density, c_p is the specific heat, $\dot{\theta}$ is the rate of temperature change, $\sigma_e\dot{\epsilon}^p$ is the plastic dissipation (σ_e equivalent stress, $\dot{\epsilon}^p$ rate of plastic strain) and χ is the plastic work conversion factor ($0 < \chi < 1$).

The above governing equations must be complemented by the constitutive equations for the sheet, as will be detailed in the next subsection.

2.2. Constitutive response of metal sheet

Two sets of constitutive equations are required to characterize the material; a set for the mechanical response relates the stress field and its rate to the strain rate, and a set for the electrical response relates the electromotive force to the current density.

[1] Here and subsequently Greek indexes range from 1 to 2 while Latin indexes range from 1 to 3. Einstein's summation convention over repeated indexes is implied, unless specified otherwise.

2.2.1. Mechanical response

During an EMF process the material experiences both high strain rates and high temperatures. Consequently a temperature-dependent viscoplastic constitutive law is required to model its stress–strain response.

The mechanical response of an incompressible material is given in rate form by

$$\mathring{\sigma}_{ij} = \mathscr{L}^e_{ijkl} D^e_{kl} + \dot{p}\delta_{ij}, \tag{2.9}$$

where $\mathscr{L}^e_{ijkl}$ are the solid's elastic moduli, D^e_{ij} are the elastic components of the strain rate tensor, $\dot{p}$ is the hydrostatic pressure rate, δ_{ij} is the Kronecker delta function (if $i = j$, $\delta_{ij} = 1$, otherwise $\delta_{ij} = 0$) and $\mathring{\sigma}_{ij}$ denotes the convected rate of Cauchy stress, i.e.

$$\mathring{\sigma}_{ij} = \dot{\sigma}_{ij} + L_{ki}\sigma_{kj} + \sigma_{ik}L_{kj}, \tag{2.10}$$

where L_{ij} is the solid's velocity gradient. Neglecting, for simplicity, thermal strains (much smaller than their elastic and plastic counterparts), one assumes the additive decomposition of strain rate into an elastic $\boldsymbol{D}^e$ and plastic $\boldsymbol{D}^p$ part, namely

$$D_{ij} = D^e_{ij} + D^p_{ij}, \tag{2.11}$$

where, for a viscoplastic solid, the plastic part of the strain rate is

$$D^p_{ij} = \dot{\epsilon}^p \frac{\partial \sigma_e}{\partial \sigma_{ij}}. \tag{2.12}$$

In the above expression ϵ^p, the accumulated plastic strain in the solid, is an internal variable that determines the size of the material's current yield surface σ_e and is related to the solid's quasistatic uniaxial response $\sigma = g(\epsilon^p, \theta)$ by

$$\dot{\epsilon}^p = \dot{\epsilon}^p_0 \left[\left(\frac{\sigma_e}{g(\epsilon^p, \theta)} \right)^{1/m} - 1 \right], \tag{2.13}$$

where m is the solid's rate-sensitivity exponent and $\dot{\epsilon}^p_0$ is a material constant. Experimentally based expressions for $\sigma_e(\sigma_{ij})$ and $g(\epsilon^p, \theta)$ will be provided subsequently.

At this point some kinematical relations are in order. The strain rate $\boldsymbol{D}$ and velocity gradient $\boldsymbol{L}$ tensor components are expressed in terms of the deformation gradient $\boldsymbol{F}$ and its rate $\dot{\boldsymbol{F}}$ by

$$D_{ij} = \frac{1}{2}(L_{ij} + L_{ji}), \quad L_{ij} = \dot{F}_{ik}F^{-1}_{kj}. \tag{2.14}$$

The sheet is assumed to be transversely isotropic, which implies that under in-plane deformations

$$F_{\alpha 3} = 0, \tag{2.15}$$

while plane stress, in conjunction with transverse isotropy and Eq. (2.14), implies

$$\sigma_{i3} = 0. \tag{2.16}$$

Incompressibility ($D_{kk} = 0$) and pressure insensitivity of the yield criterion ($\partial\sigma_e/\partial\sigma_{kk} = 0$) result in the plane stress version of the constitutive equation (2.9), namely

$$\mathring{\sigma}_{\alpha\beta} = \hat{\mathscr{L}}^{e}_{\alpha\beta\gamma\delta} D^{e}_{\gamma\delta}, \tag{2.17}$$

where the plane stress elastic moduli $\hat{\mathscr{L}}^{e}_{\alpha\beta\gamma\delta}$ are given in terms of their full three-dimensional counterparts by

$$\hat{\mathscr{L}}^{e}_{\alpha\beta\gamma\delta} = \mathscr{L}^{e}_{\alpha\beta\gamma\delta} - \delta_{\alpha\beta}\mathscr{L}^{e}_{33\gamma\delta} - \mathscr{L}^{e}_{\alpha\beta33}\delta_{\gamma\delta} + \mathscr{L}^{e}_{3333}\delta_{\alpha\beta}\delta_{\gamma\delta}. \tag{2.18}$$

The constitutive model for the temperature-dependent, incompressible viscoplastic model presented thus far requires two additional experimentally obtained pieces of information to be complete: the rate-independent uniaxial response $\sigma = g(\epsilon^{p}, \theta)$ and the yield surface $\sigma_e(\sigma_{ij})$.

The rate-independent uniaxial response adopted in the calculations is of the form (see [17])

$$g(\epsilon^{p}, \theta) = \sigma_y \left[1 + \frac{\epsilon^{p}}{\epsilon_y}\right]^{n} \left[1 - \left(\frac{\theta - \theta_0}{\theta_m - \theta_0}\right)^{\alpha}\right], \tag{2.19}$$

where n is the hardening exponent, α the thermal sensitivity, σ_y the yield stress, $\epsilon_y = \sigma_y/E$ the yield stain, θ_m the melting temperature and θ_0 the reference temperature. For isotropic materials that do not exhibit the Bauschinger effect, i.e. materials that exhibit no difference between their tensile and compressive responses, the following yield surface criterion (e.g. Barlat et al. [18] and references quoted therein.) is used

$$\sigma_e = \left[\left(|\sigma_1 - \sigma_2|^{\beta} + |\sigma_2 - \sigma_3|^{\beta} + |\sigma_3 - \sigma_1|^{\beta}\right)/2\right]^{1/\beta}, \tag{2.20}$$

where β is an experimentally determined exponent and σ_i are the principal values of the Cauchy stress tensor. The mechanical constitutive response of the solid is thus completely determined by Eqs. (2.9)–(2.20). Uniaxial and plane stress biaxial experiments are employed for the selection of the material constants used in the subsequent simulations.

2.2.2. Electrical response

The material's electric constitutive law, i.e. the relation between current $\boldsymbol{j}$ and electromotive force $\boldsymbol{e}$, is taken to be an isotropic Ohm's law

$$e_i = r j_i, \tag{2.21}$$

where the resistivity of the metal r is assumed to be temperature-independent for the temperature range of interest. The electric constitutive equation is completed in a thin sheet by

$$j_3 = 0, \tag{2.22}$$

since the current in the sheet can flow only in its plane.

All the governing equations that are required for the calculations of the field quantities inside the band, given the knowledge of their counterpart outside the band, have been established. The numerical solution procedure of the above-presented algebraic equations is postponed to Section 3.

2.3. Experimental procedure

Fig. 2 shows a schematic of the set-up for the electromagnetic tube expansion experiments. It consists of a capacitor bank connected to a solenoid actuator placed inside an aluminum alloy tube. The experiments are conducted using a commercial Maxwell Magneform capacitor bank with a maximum stored energy of 16 kJ. The energy is stored in eight capacitors, each with a capacitance of 53.25 μF. The system has a maximum working voltage of 8.66 kV. Both the number of capacitors and charging voltage can be adjusted to control the discharged energy. One Rogowski probe, R1 in Fig. 2, is used to measure the primary current. A second such probe, R2 in Fig. 2, measures the aggregate coil current, which is the product of the number of coil turns and the primary current, combined with the induced current in the tube.

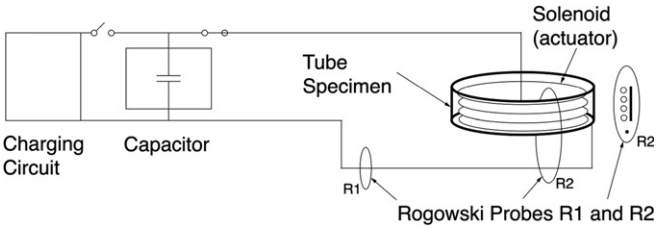

Fig. 2. Schematic representation of the experimental set-up for electromagnetic expansion of tubes.

Fig. 3a shows one of the bare coils fabricated by commercial spring winding from 6.35 mm diameter ASTM B16 brass wire. Two coils are used in these experiments, one with four turns (as shown in Fig. 3a) and an otherwise identical coil with ten turns. Both coils have an outer diameter of 54 mm and pitch of 9.4 mm. The wire is covered with heat shrink-wrap tubing to provide insulation and then potted in urethane. Fig. 3b shows the actual experimental configuration with an aluminum alloy tube sample fitted over the epoxy-coated coil. The tube samples are AA6063-T6 aluminum alloy with an inner diameter of 57 mm and a wall thickness of 1.75 mm. The outer surface of each tube is electrolytically etched with a pattern of 2.5 mm diameter circles in order to measure the strain in the expanded samples.

For each combination of coil and sample size, multiple samples are expanded with incrementally increasing discharge energies until an energy level sufficient to initiate necking and/or fracture of the tube is reached. Major and minor limit strains are then measured from the deformed circles in areas where necking occurs, labeled "Unsafe", and in areas where no necking or failure is evident, labeled "Safe". Fig. 4 shows a sample deformed tube for each of the four possible combinations of tube length and coil length. The short coil is approximately the same length, 31.7 mm, as the short tubes; the long coil is about the same length, 85.1 mm, as the long tubes. In Fig. 4, tubes (a) and (b) are short while tubes (c) and (d) are long, and tubes (a) and (c) are deformed using a 4-turn coil while tubes (b) and (d) are deformed using a 10-turn coil. The data gathered will subsequently be compared with the onset of necking calculations described above. Full details of these experiments are published in Seth [19].

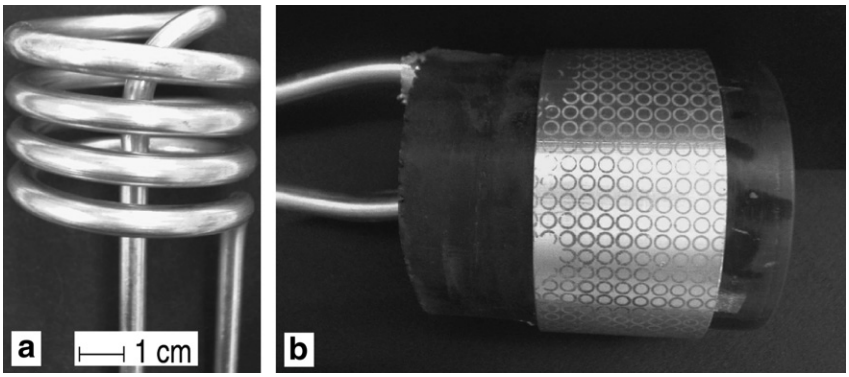

Fig. 3. (a) The bare 4-turn coil. (b) Sample-actuator configuration. The 31.7 mm tall aluminum tube sample is shown fitted around the urethane-coated 4-turn coil.

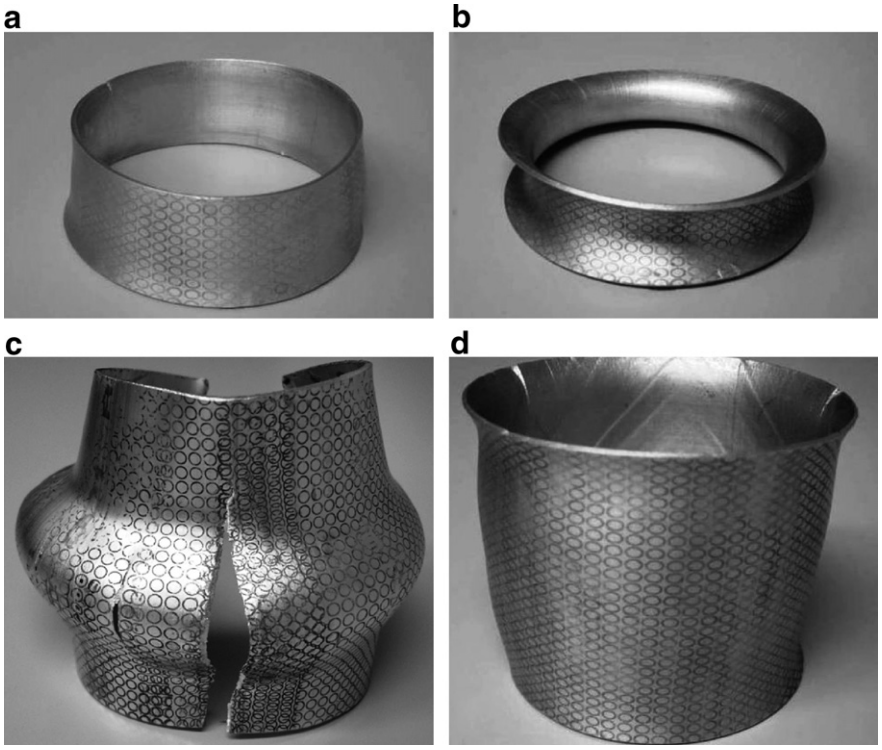

Fig. 4. Final configuration showing localized necking of tubes deformed using the experimental EMF setup. (a) 31.7 mm tube deformed with 4-turn coil, (b) 31.7 mm tube deformed with 10-turn coil, (c) 85.1 mm tube deformed with 4-turn coil and (d) 85.1 mm tube deformed with 10-turn coil.

In addition, data on the tube material's uniaxial quasistatic stress–strain response are gathered using an MTS machine. Samples are cut from the AA6063-T6 tubes according to the ASTM tensile sample standard (0.630 cm wide, 2.54 cm long) by water jet. Tests are conducted at a strain rate of $3.3 \times 10^{-3}\ s^{-1}$, and the uniaxial quasistatic stress–strain response in Eq. (2.19) (with constant temperature $\theta = \theta_0$) is fit with data corresponding to a sample cut longitudinally from the tube (transverse samples are omitted since the curvature of the tube requires substantial straightening, altering the material's behavior in the test). Fig. 5 gives a comparison of the experimental data and analytical fit. The resulting material parameters are detailed below.

2.4. Selection of material constants

The electromagnetically expanded tubes are made of AA6063-T6, a tube alloy. However, material constants required for the determination of the quasistatic FLD are obtained from experiments using flat sheet blanks. In addition, an independent measurement of rate and thermal sensitivity parameters, at the strain rates and temperatures of interest, requires highly specialized equipment that is not available to us. The strategy adopted to address these issues is to use uniaxial quasistatic test measurements from AA6063-T6 to obtain the values of Young's modulus E, yield stress σ_y and hardening exponent n and to rely on existing independent experiments on a closely related alloy,

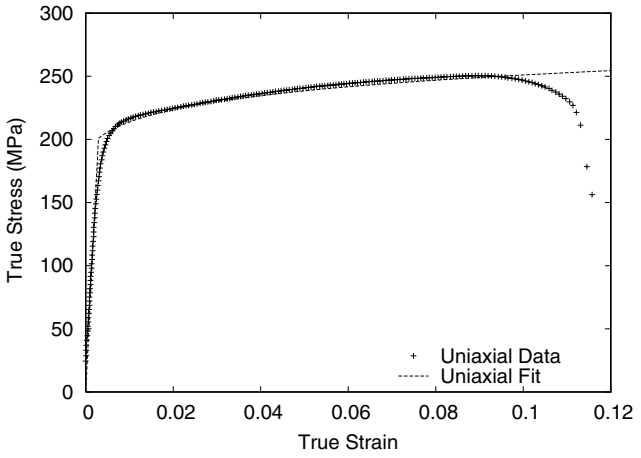

Fig. 5. AA6063-T6 uniaxial quasistatic stress–strain response: experimental data and corresponding theoretical fit.

AA6061-T6, for which the remaining required material parameters have been published. From uniaxial tests on thin strips cut longitudinally from AA6063-T6 tubes, the best fit (see Fig. 5) is achieved using the values in Table 1.

The remaining parameters are obtained from different sources. The rate and thermal sensitivity related parameters are based on experiments by Yadav et al. [14,17] and are given in Table 2.

The mass density, thermal and electrical properties are obtained from standard references on aluminum (they are not alloy sensitive) and are given in Table 3. The value of the plastic work conversion factor χ is the same as in Triantafyllidis and Waldenmyer [3].

The remaining parameters to be determined pertain to the characterization of the yield surface and the size of the imperfection amplitude ξ. To this end the band is modeled by a discontinuity in the yield stress, using $\sigma_y^B = (1-\xi)\sigma_y^A$. The yield surface exponent β (see definition in Eq. (2.20)) is taken as in Barlat et al. [18] for aluminum, and the value of ξ is then chosen to give the most reasonable agreement with the available quasistatic FLD experiments on AA6061-T6 by LeRoy and Embury [20], as shown in Table 4. The parameters given in Tables 1–4 completely characterize the mechanical, thermal and electric properties of the model used to run the simulations of the free expansion experiments of the tubes.

Table 1
Material parameters from AA6063-T6

$E = 69$ GPa	$\sigma_y = 190$ MPa	$\epsilon_y = \sigma_y/E$	$n = 0.0769$

Table 2
Material parameters from AA6061-T6 [17]

$\dot{\epsilon}_0^p = 1000\ s^{-1}$	$m = 0.0870$	$\alpha = 0.5$	$\theta_0 = 298$ K	$\theta_m = 853$ K

Table 3
Density, specific heat, resistivity of aluminum and conversion factor

$\mu = 2700\ kg/m^3$	$c_p = 896$ J/kg K	$r = 2.65 \times 10^{-8}\ \Omega m$	$\chi = 0.9$

Table 4
Material parameters for FLD of AA6061-T6

$\beta = 8$	$\xi = 10^{-3}$

2.5. Strain, strain rate and current density profiles

Calculations of FLDs for strain rate-independent elastoplastic solids are frequently based on the simplifying assumption of proportional strain paths. It is assumed that $\epsilon_2/\epsilon_1 = \dot{\epsilon}_2/\dot{\epsilon}_1 = \rho$, where $-1/2 \leqslant \rho \leqslant 1$ with the lower limit corresponding to uniaxial stress and the upper to equibiaxial plane stress. The time dependence of strain ϵ_1 (or ϵ_2) is irrelevant for predicting FLDs under quasistatic loading of rate-independent solids. For the time-dependent viscoplastic response of the material in EMF processes, strain history influences the solid's response and hence a strain profile $\epsilon_1(t)$ is also required (the proportional straining assumption $\epsilon_2(t) = \rho\epsilon_1(t)$ is still assumed). Determining the exact strain profile $\epsilon_1(t)$ requires solution of a coupled electromagnetic and thermomechanical problem of the tube plus its actuator coil, a feasible but complicated and time-consuming task. Such a modeling approach would be the two-dimensional version of the one-dimensional ring calculations done by Triantafyllidis and Waldenmyer [3]. In the interest of simplicity, and since a pulse-like strain rate history is expected for the hoop strains at any height of the expanding tube, the following sinusoidal-shape strain rate pulse is assumed

$$\dot{\epsilon}_1(t) = \frac{\pi\epsilon_{\max}}{8\tau_0}\sin\left(\frac{\pi t}{4\tau_0}\right), \quad \dot{\epsilon}_2(t) = \rho\dot{\epsilon}_1(t), \tag{2.23}$$

where $4\tau_0$ is the duration of the strain rate pulse and $\epsilon_{\max}$ is the maximum strain in the hoop direction since from Eq. (2.23)

$$\epsilon_1(t) = \frac{\epsilon_{\max}}{2}\left[1 - \cos\left(\frac{\pi t}{4\tau_0}\right)\right]. \tag{2.24}$$

The electromagnetic nature of the problem also requires knowledge of the time-dependent current density. Again a sinusoidal pulse current density is assumed in the hoop direction

$$j_1(t) = J_{\max}\sin\left(\frac{\pi t}{2\tau_0}\right), \quad j_2(t) = 0, \quad j_i = 0 \text{ for } t > 2\tau_0, \tag{2.25}$$

where $J_{\max}$ is the maximum current density achieved in this process. Experimental observations, as well as fully coupled electromechanical calculations in the ring problem [3], show that the time duration of the first (and much larger) current pulse is approximately half the duration of the strain rate pulse, thus explaining the reason for the choice in Eq. (2.25).

The characteristic time τ_0, which is half of the measured duration of the main current pulse, and the maximum density J_{max} are available experimentally, according to Table 5. These parameter values are obtained from electric current vs. time traces taken from tube expansion experiments. An example of one of these traces, here from case (a), is shown in Fig. 6a. The comparison between experimental and simulation current traces is shown in Fig. 6b, along with the dimensionless strain vs. time trace. The energy used to expand the tube in each configuration is given in Table 5, and the pulse time τ_0 and maximum current density J_{max} used in the corresponding simulation are also listed accordingly. Also note that from several experiments performed, only four (labeled a, b, c, d in Table 5) are to be simulated here.

Table 5
Experimentally determined parameters

Label	Tube (mm)	Coil	Energy (kJ)	J_{max} (A/m^2)	τ_0 (μs)
a	31.7	4-turn	6.72	5.10×10^9	23
b	31.7	10-turn	8.00	4.82×10^9	36
c	85.1	4-turn	7.52	2.50×10^9	16
d	85.1	10-turn	13.92	4.85×10^9	33.5

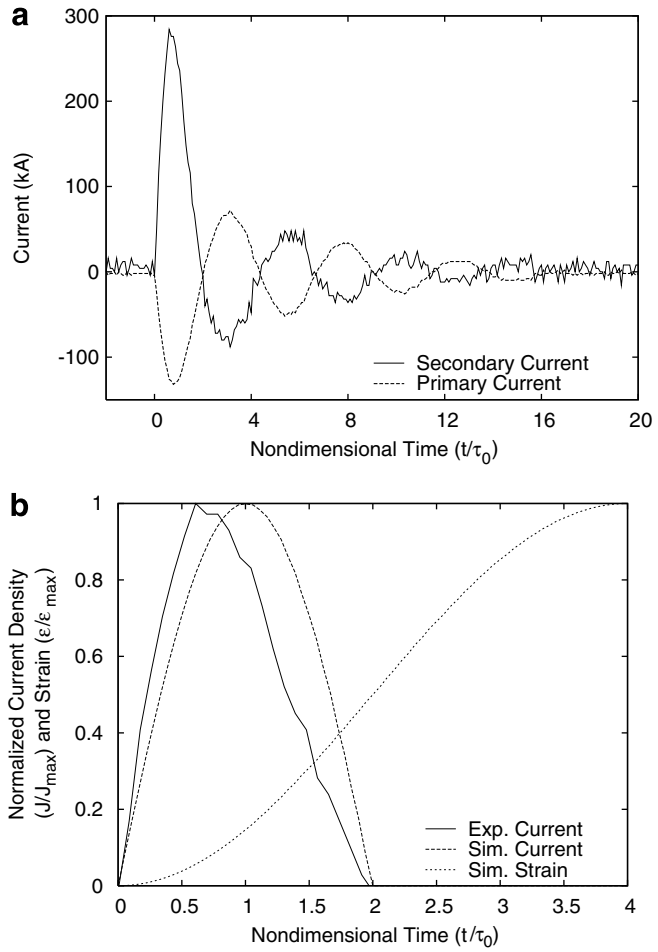

Fig. 6. (a) Example of an experimentally measured current vs. time trace for tube and coil. (b) Comparison of the experimentally determined current density profile with the simulated current density profile. Simulated dimensionless strain profile also shown in (b). These plots correspond to a 31.7 mm tube deformed with a 4-turn coil at 6.72 kJ of energy (case (a)).

The final issue to be resolved is the choice of the maximum hoop strain ϵ_{max} in Eq. (2.24) for simulating the selected four experiments. The choice adopted stems from the experimental technique of gradually increasing the capacitor energy until tube necking and/or failure is detected. Consequently, for each ρ a simulation is run with a certain value of ϵ_{max} for which no necking is detected. A simple forward marching technique gradually tests larger values of ϵ_{max} until necking is achieved at $0.99\epsilon_{max}$. As an example of the forming speeds that result from this technique, for case (a) in Table 5 the maximum simulation strain rate ranges from 4932 s^{-1} (plane strain) to 8793 s^{-1} (uniaxial).

3. Results and discussion

The formulation of the EMF localization problem has been fully defined above. It is now left to detail the numerical algorithm used to solve the governing equations, to compare the theoretical simulations with the experiments and to comment on the results.

3.1. Numerical algorithm

The governing equations for the principal solution and for the localization problem can be cast as a system of first-order ordinary differential equations (ODEs) $\dot{x} = f(x,t)$. A fourth-order Runge–Kutta algorithm is used for each case. More specifically, for each path (for given ρ), the principal solution requires the solution of a system of four ODEs

$$\dot{x}_A = f(x_A,t), \quad x_A \equiv [\sigma_1^A, \sigma_2^A, \epsilon_A^p, \theta^A], \tag{3.1}$$

where σ_1, σ_2 are the hoop and axial Cauchy principal stresses, ϵ^p is the accumulated plastic strain and θ is the temperature of the sheet. For the localization problem along each path, a much larger system of nine ODEs has to be solved for each value of the reference localization angle Φ, namely

$$\dot{x}_B = f(x_B,t),$$
$$x_B \equiv [F_{11}^B, F_{12}^B, F_{21}^B, F_{22}^B, \sigma_{11}^B, \sigma_{12}^B, \sigma_{22}^B, \epsilon_B^p, \theta^B], \tag{3.2}$$

where the t-dependent terms in $f(x_B,t)$ are functions of the principal solution $x_A(t)$. Note that j_i^B are obtained directly from Eqs. (2.4)–(2.7) and (2.21). The rate forms of Eqs. (2.1) and (2.2) are used due to the inherent incremental nature of plasticity calculations.

For each load path (i.e. given ρ, τ_0, J_{max}, ϵ_{max}), a value of the localization angle Φ is selected in the interval $0 \leqslant \Phi < \pi/2$. Necking is detected when the plastic strain rate inside the band becomes unbounded. In the numerical simulations necking is said to occur at t_{neck}, the time when $\dot{\epsilon}_B^p/\dot{\epsilon}_A^p > 10$, and $\epsilon_{neck} \equiv \epsilon_1^A(t_{neck})$ (the choice of value 10,

although arbitrarily selected, has negligible effect on the localization strain). The entire Φ range $0 \leqslant \Phi < \pi/2$ is scanned using $\pi/180$ increments and the critical angle Φ is the one minimizing $\epsilon_{\text{neck}}(\Phi)$. As in the quasistatic case, $\Phi \neq 0$ for $\rho < 0$ while $\Phi = 0$ for $\rho \geqslant 0$. Calculation of the critical angle Φ will be discussed subsequently.

Two checks on the solution are used to select the step size Δt. For the quasistatic case an analytical solution is known for certain values of ρ. The step size is chosen small enough that the simulation results match the analytical solution within a reasonable accuracy (0.001, i.e. forming limits accurate to within 0.1% true strain). For the rate-dependent case numerical errors are avoided by decreasing Δt until the change in solution from an additional decrease in Δt is within the required accuracy. This approximately gives $\Delta t/\tau_0 \approx 5 \times 10^{-5}$ as the typical time step, to which adjustments are made as necessary.

3.2. Comparison of experimental and theoretical results

The presentation of experimental results and the corresponding theoretical simulations is given in Figs. 7–12. More specifically the experimentally obtained FLDs for cases (a)–(d) (see Table 5) plus the corresponding theoretical simulation results are presented in Figs. 7, 10, 11 and 12 respectively. For comparison purposes the conventional quasistatic FLDs for the same cases (calculated in the absence of currents and using much larger pulse duration times τ_0) are also plotted in these figures to show the ductility increase due to the EMF process. Additional information for the first experiment (case (a)) is provided in Fig. 8 (current configuration localization angle ϕ vs. strain ratio ρ) and Fig. 9 (temperatures inside θ^B and outside θ^A the band vs. strain ratio ρ).

The FLD results for the short tube/short coil combination (case (a)) are presented in Fig. 7. Notice that the experimental data are all for $\rho < 0$ and are clustered about the uniaxial stress path ($\rho = -1/2$), as expected from Fig. 4a,

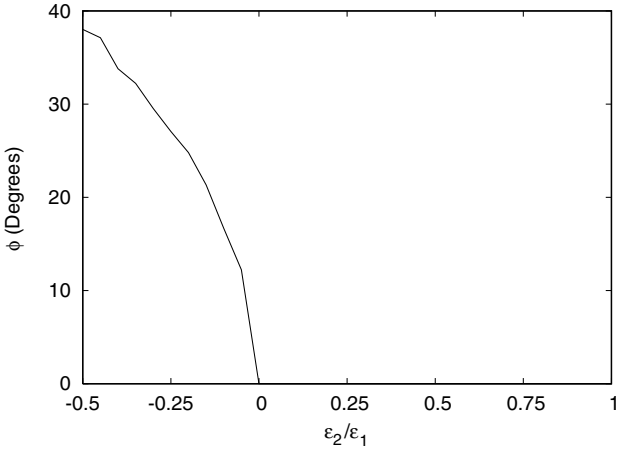

Fig. 8. The localization angle ϕ in the current configuration as a function of strain ratio ρ, for the simulation of the 31.7 mm tube deformed with a 4-turn coil at 6.72 kJ (case (a)).

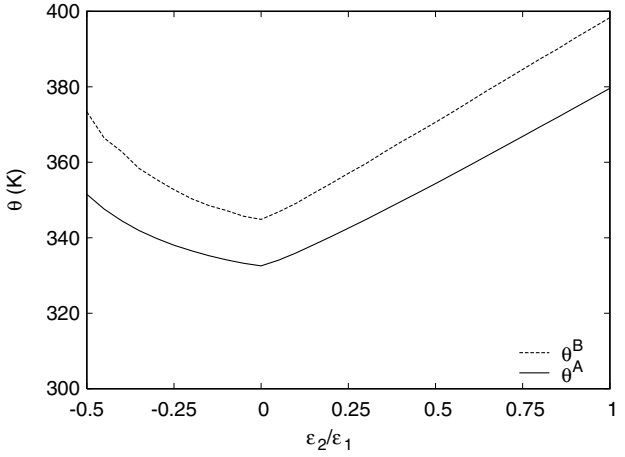

Fig. 9. The temperature inside θ^B and outside θ^A the band at localization as a function of principal strain ratio ρ, for the simulation of the 31.7 mm tube deformed with a 4-turn coil at 6.72 kJ (case (a)).

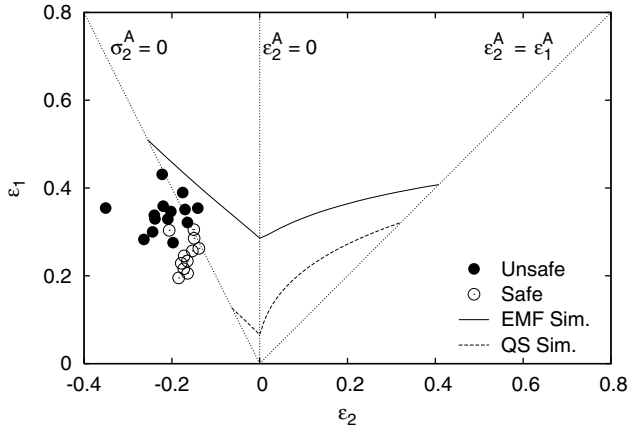

Fig. 7. Comparison of simulated and experimental forming limits for an AA6063-T6 31.7 mm tube deformed using a 4-turn coil and 6.72 kJ of energy (case (a)).

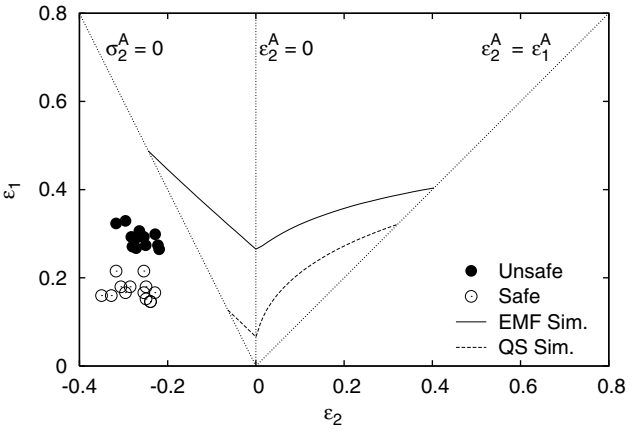

Fig. 10. Comparison of simulated and experimental forming limits for an AA6063-T6 31.7 mm tube deformed using a 10-turn coil and 8 kJ of energy (case (b)).

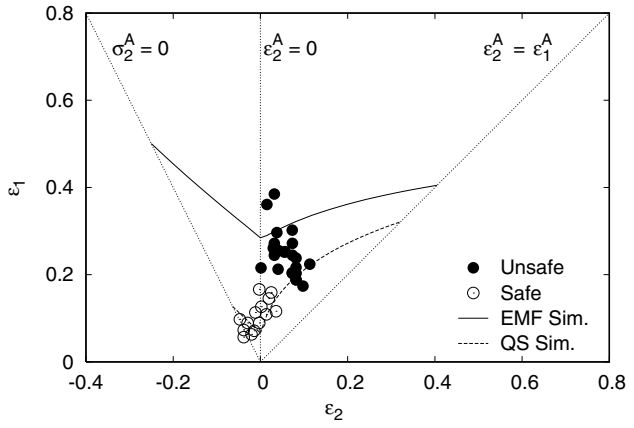

Fig. 11. Comparison of simulated and experimental forming limits for an AA6063-T6 85.1 mm tube deformed using a 4-turn coil and 7.52 kJ of energy (case (c)).

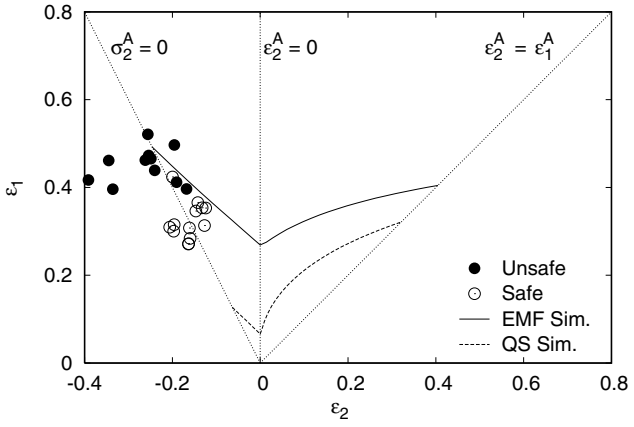

Fig. 12. Comparison of simulated and experimental forming limits for an AA6063-T6 85.1 mm tube deformed using a 10-turn coil and 13.92 kJ of energy (case (d)).

which shows localization at the top and bottom ends of the short tube. Both the measured and computed results show a significant increase in ductility in the electromagnetically expanded AA6063-T6 tube compared to the quasistatic curve, although the simulation overestimates the forming limits. Moreover, using Fig. 5 one can observe that uniaxial quasistatic AA6063-T6 necking and failure occur approximately at $\epsilon_{\text{neck}} = 0.11$. This corresponds to the $\rho = -1/2$ quasistatic forming limit in Fig. 7 due to the use of rectangular high aspect ratio (width to thickness) samples in the uniaxial quasistatic tests (see Section 2.3). This observation is an experimental confirmation of the ductility increase in free forming using EMF, which is captured reasonably well by the present simulation.

The theoretically calculated current configuration critical angle ϕ vs. the strain ratio ρ for the short tube/short coil experiment modeled in Fig. 7 is plotted in Fig. 8. Notice that similar to the quasistatic case, ϕ is a decreasing function of ρ for $-1/2 \leqslant \rho < 0$, while $\phi = 0$ for $\rho \geqslant 0$. Although localization angles are difficult to measure, where the necking band is visible along the full length of the tube (case (d), corresponding to $\rho = -1/2$), $\phi \approx 40°$.

The theoretically calculated inside θ^B and outside θ^A the band respectively temperatures at localization, as a function of strain ratio ρ for the experiment modeled in Fig. 7, are plotted in Fig. 9. Notice that the necking temperature is minimum for $\rho = 0$, as expected from the fact that the critical strain, ϵ_1, is a minimum here. Since τ_0 is kept constant for each case, the minimum critical strain gives the minimum strain rates and lowest flow stresses and thus the lowest amount of plastic dissipation $\sigma_e \dot{\epsilon}^p$. This dissipation contributes somewhat more thermal energy than the ohmic effect to the temperature change [3].

Figs. 10–12 show the results from the remaining three experiments (see Table 5 and also Fig. 4). More specifically Fig. 10 shows the results for the shorter tube with the longer coil (case (b)), which shows the largest discrepancy between theory and experiment. This deviation can be explained from the fact that the failed tube in Fig. 4b is a highly distorted toroidal segment, while the assumptions adopted for the computation of the FLD are based on uniformly expanding tubes.

The FLD in Fig. 11 corresponds to the only experiment with data in the $\rho > 0$ region, as expected for case (c), in Fig. 4c, where failure starts at the middle of the tube. Experimental points on $\rho = 0$ show agreement with theoretical predictions, while experimental points for $\rho > 0$ show large deviations from theoretical results. This discrepancy is expected from the fact that yield surface parameters and anisotropy of sheet play a crucial role for the determination of the $\rho > 0$ part of the FLD, and our simulation's simplified isotropic yield surface can be improved with a more sophisticated anisotropic alloy description. Moreover, as with case (a), despite overestimation of the forming limits, a free formability increase is clearly shown experimentally.

Finally, Fig. 12 corresponds to the long tube/long coil combination and the corresponding experimental data are again clustered around the uniaxial stress path $\rho = -1/2$, as expected from Fig. 4d, which shows failure near the end sections of the tube. This comparison shows the closest agreement between experiment and simulation, with the forming limits minimally overestimated.

It should be noted that the theoretical predictions for all four experiments are predictably close to each other given the proximity of the values of the strain rates, current densities and characteristic times between the four different experiments. A critical discussion of the experimental and theoretical results is given below.

3.3. Comments and discussion

For the free expansion experiments, the main reason for the increased ductility of aluminum alloys has been shown [3] to be their strain rate sensitivity at the high rates associated with the EMF processes. To this end, it is important to obtain an accurate constitutive description of the alloy

that has strain rate as well as temperature sensitivity in its mechanical response, given the important heating effects due to the plastic dissipation and the induced currents. Although it was not possible to measure all the required constitutive properties of the experimentally used (AA6063-T6) tube alloy, a careful literature search has given the remaining properties from reliable, independently obtained data of a closely related (AA6061-T6) sheet alloy. Implementing these properties shows an increase in formability due to rate sensitivity in the FLD simulations, which is confirmed experimentally. However, comparing experiment to simulation shows overestimation to varying degrees in each forming limit diagram. A more accurate experimentally based constitutive characterization of the material is necessary for further investigations.

There are additional limitations to our model. Inertia is ignored in these necking simulations. In previous unpublished work on ring expansion [21] an increase in ductility occurred with an increase in ring density (with all other ring properties remaining the same). More sophisticated dynamic stability analyses have been carried out for bars [4] and rings [8] that show how inertia determines the critical wave number, influencing (delaying) necking. Other work [5,7,11] has shown similar results, indicating that inertia should be accounted for in dynamic necking calculations.

Furthermore, the present work considers only tube free expansion, while others [6,9,10] have considered different geometries. Oliveira and Worswick [9] and Oliveira et al. [10] considered forming aluminum sheet into a rectangular die opening. No formability improvement in their electromagnetically free formed parts was reported. Those authors showed EMF strains higher than the quasistatic forming limits but attributed them to strain path changes after workpiece failure. However, Imbert et al. [6] did show EMF free forming strains above the traditional quasistatic limits of their aluminum alloy on safe (no necking or failure) parts. Those experiments used aluminum sheet free formed into a circular die opening and indicated that EMF may enhance free formability. It should be noted that the electromagnetic process free forming strain rates of Oliveira and Worswick [9] and Oliveira et al. [10] are approximately half the rates encountered in the present experiments, and the aluminum alloy used in these earlier experiments was AA5754, which is considerably different from our tube alloy AA6063-T6. Work by Vural et al. [13] and Yadav et al. [14] showed a distinct alloy-dependent threshold above which strain rate sensitivity becomes important, indicating these differences may significantly influence the experiments.

4. Conclusion

Electromagnetic forming (EMF) processes are known to increase significantly the ductility of aluminum alloys. The goal of the present work is a quantitative comparison between theoretical calculations for the onset of necking in sheets and the experimental results obtained from the free expansion of electromagnetically loaded aluminum alloy tubes on which strain-measuring grids have been etched. Although a fully coupled electromagnetic and finite strain thermomechanical analysis is required to accurately model the tube expansion experiments, considerable insight can be gained by using the recently proposed [16] electromagnetic generalization of the forming limit diagram (FLD) concept to study the ductility of aluminum sheets, as measured locally in the necked regions of the failed tubes.

In conclusion, and given the approximations inherent in the FLD concept (essentially the assumed strain and current paths which can differ substantially from the actual ones at the necked zone), there is agreement between theory and experiment, showing that the ductility increases in free forming due to the use of an EMF process. Most of the specimens fail near the rims, thus justifying the clustering of the experimental data near the $\rho = -1/2$ line of the FLD. When failure occurs about the midpoint of the tube's generator, there is a bigger spread of experimental points, this time about the $\rho = 0$ path. In this case there is again reasonable correlation between simulation and experimental data. The present comparison between theory and experiments shows that the EMF-based FLD concept is a useful tool to predict ductility limits of metal sheet in free expansion experiments.

Acknowledgements

J.D. Thomas, M. Seth, G.S. Daehn and N. Triantafyllidis gratefully acknowledge support by the General Motors Research & Development. The work of J.D. Thomas and N. Triantafyllidis is partially supported by NSF grant DMI 0400143. J.D. Thomas and N. Triantafyllidis also gratefully acknowledge helpful discussions with Professor G. Ravichandran of the California Institute of Technology.

References

[1] Balanethiram V, Daehn GS. Scr Met Mater 1992;27:1783.
[2] Balanethiram V, Daehn GS. Scr Met Mater 1994;30:515.
[3] Triantafyllidis N, Waldenmyer J. J Mech Phys Solids 2004;52:2127.
[4] Fressengeas C, Molinari A. Inst Phys Conf Ser 1989;102:57.
[5] Hu XY, Daehn GS. Acta Mater 1996;44(3):1021.
[6] Imbert JM, Winkler SL, Worswick MJ, Oliveira DA, Golovashchenko S. J Eng Mater – T ASME 2005;127:145.
[7] Knoche P, Needleman A. Eur J Mech A – Solid 1993;12(4):585.
[8] Mercier S, Molinari A. Int J Impact Eng 2004;30(4):403.
[9] Oliveira DA, Worswick M. J Phys IV France 2003;110:293.
[10] Oliveira DA, Worswick MJ, Finn M, Newman D. J Mater Process Tech 2005;170:350.
[11] Regazzoni G, Johnson JN, Follansbee PS. J Appl Mech – T ASME 1986;53(3):519.
[12] Oosterkamp DL, Ivankovic A, Venizelos G. Mater Sci Eng A 2000;278:225.
[13] Vural M, Rittel D, Ravichandran G. High strain rate behavior of metal alloys at large strains. GALCIT Report. Graduate Aeronautical Laboratories, The California Institute of Technology, Pasadena, CA; 2004.
[14] Yadav S, Chichili D, Ramesh K. Acta Met Mater 1995;43:4453.

[15] Rittel D, Ravichandran G, Lee S. Mech Mater 2002;34:627.
[16] Thomas JD, Triantafyllidis N. Int J Solids Struct, to appear.
[17] Yadav S, Repetto EA, Ravichandran G, Ortiz M. Int J Impact Eng 2001;25(8):787.
[18] Barlat F, Maeda Y, Chung K, Yanagawa M, Brem J, Hayashida Y, et al. J Mech Phys Solids 1997;45:1727.
[19] Seth M. PhD thesis. The Ohio State University, Materials Science and Engineering Department, 2006.
[20] LeRoy G, Embury JD. In: Hecker SS, Ghosh AK, Gegel HL, editors. Formability analysis, modeling, and experimentation. New York, NY: AIME; 1978. p. 183.
[21] Triantafyllidis N. Unpublished work 2004.